Eur. Phys. J. B **41**, 485–493 (2004)
DOI: 10.1140/epjb/e2004-00342-3

THE EUROPEAN PHYSICAL JOURNAL B

Quantitative analysis of gold nanoparticles from synchrotron data by means of least-squares techniques

Least-squares analysis of gold nanoparticles

A. Cervellino[1,a], C. Giannini[1], A. Guagliardi[1,b], and D. Zanchet[2]

[1] Consiglio Nazionale delle Ricerche, Istituto di Cristallografia (CNR-IC), Via Amendola 122/O, 70125 Bari, Italy
[2] Laboratorio Nacional de Luz Sincrotron (LNLS), C.P. 6192, 13084-971 Campinas SP, Brazil

Received 23 June 2004
Published online 5 November 2004 –

Abstract. Powder samples of thiol-capped gold nanoparticles in the size range of 2–4 nm were quantitatively characterized by means of synchrotron X-ray diffraction data, with respect to their structure, size and strain distributions. A novel Rietveld-like approach was applied, refining domain size distribution, strain-size dependence and structure type concentrations. Three structure types (cuboctahedron, icosahedron, decahedron) were considered in this analysis and a detail study of the strain content was performed by comparing different models. The results showed a strong influence of the strain model and a careful analysis is presented. Final domain size and strain distributions agree well with the existence of both single-domain and imperfectly formed or multi-domain nanoparticles, but the final strain profiles seem to be mostly related to the different degree of structural perfection at different sizes as a result of the synthesis process. The present work represents an important step towards the development of robust methods to determine strain profiles in nanosystems, aiming to fulfill the description of these important but complex systems.

PACS. 81.07.-b Nanoscale materials and structures: fabrication and characterization – 61.10.Nz X-ray diffraction – 61.72.Dd Experimental determination of defects by diffraction and scattering

1 Introduction

The interest in nanomaterials research has been increasing in the last decades due to their potential exploitation in new revolutionary technologies. In particular, size-related effects have been explored to tune materials properties and to produce unique systems. It has been a key point to understand the size reduction effects and for that, new methodologies have to be continuously improved. In particular, the control of basic features of synthesized nanoparticles (NPs), such as well characterized crystalline domains, narrow size and shape distributions, are fundamental for any efficient application.

From the structural point of view, important discoveries have taken place. One may recall the milestone works from Ino [1–4] about the occurrence of non-crystallographic structure types in Au nanoparticles, besides the typical face-centered cubic (fcc) bulk. Further works have confirmed that deep structural modifications may occur in nanoparticles and a good review of pre-1994 work can be found in [5]. We cite here only few examples especially regarding metal nanoclusters, such as gold [6–9], silver [10, 11] or cobalt [12–15]. Gold nanoparticles received special attention; major interest topics include: non-crystallographic structure types [5, 16–19]; size-dependent strain effects [16, 20, 21]; importance of defects [5, 17], and cluster amorphization [22].

Due to the complexity and newness of nanomaterials, combinations of different techniques are usually required, such as X-ray Diffraction (XRD), Small Angle X-ray Scattering (SAXS), Extended X-ray Absorption Fine Structure (EXAFS) and High Resolution Transmission Electron Microscopy (HRTEM). Equally important is the association with continuously improved methodology for data analysis. In particular, due to the major importance of surface energy at small sizes (see [3–5, 23] and references therein), large strain effects are usually present and affect XRD signal[1]. The conventional XRD analysis does not work well for nanoparticles due to the intrinsic peak broadening and other size reduction effects. In fact,

[a] *On leave. Presently at:* Paul Scherrer Institute, 5232 Villigen, Switzerland
[b] e-mail: antonella.guagliardi@ic.cnr.it

[1] Among the mentioned experimental techniques, XRD and EXAFS are both very sensitive to strain in nanosystems, while SAXS and HRTEM are not.

a suitable representation of the strain contained in NPs or its dependence with particle size is still a challenge for most analytical tools.

To address this aspect, an original quantitative method based on a Rietveld-like approach was previously described in [19], dealing with monoatomic fcc-derived metallic NPs. The effectiveness of the method to accurately estimate structure and size/strain distributions was tested mainly on simulated patterns of gold nanoparticles. The present report contains the application of the method to synchrotron data (see Sect. 2) of three specimens of thiol-capped gold crystals in the size range of 2–4 nm [17]. The main features of the data analysis method, together with the last model and algorithm evolutions, are summarized in Section 3. Our gold thiol-capped samples had been analyzed in a previous work [17] by XRD and HRTEM techniques, with respect to their size and structure population but without a detailed strain content investigation. EXAFS results [24] on the same samples highlighted a very small reduction of the nearest-neighbour distance as a function of particle diameter; this was assigned to the presence of thiol molecules on particles' surface.

Despite some efforts, a lack of a detail quantitative strain analysis in nanoparticles still exists in the literature. In the present paper, an extensive strain analysis was performed within the approximation of the strain model included in the method. During the strain analysis, as described in Section 4, the results pointed out the need of a better background description and an amorphous metal scattering contribution was included. This has been shown essential to obtain high-quality fits and reliable parameter estimates. The final refinement results are presented and discussed in Section 5, followed by conclusions in Section 6. For an extensive description of the model see [19] and references therein.

2 Experimental

Three samples of thiol-passivated gold nanoparticles were synthesized as described in [17] and the size distributions were characterized by HRTEM. The mean diameters were 2.0, 3.2 and 4.1 nm, respectively with FWHM of about 1 nm for all cases. In this work, we refer to the samples by their HRTEM mean diameters. Powder XRD patterns were collected at the Brazilian Synchrotron Light Laboratory (LNLS-Campinas, Brazil) using a Si(111) double crystal to monochromatize the incident X-ray beam (8.040 KeV), at room temperature and with a wide detection slit (2 mm) in front of the scintillation detector. The sample was measured in a flat-plate configuration with the oily powder spread onto a glass substrate. The experimental resolution was about 0.13°, which is much smaller than particle-size broadening in this size range. In fact, 4.1 nm spherical fcc-Au nanoparticles are expected to show a 2.5° FWHM at the (111) peak. The 2θ angular range from 20° up to ≈150° was measured with a 2θ step ≈0.2°. The wavelength corresponds to $\lambda = 0.1542$ nm with an estimated error of ±0.5%, allowing for 40 eV uncertainty in beam energy. The wavelength error was taken into account when calculating standard deviations on strain parameters. The beam energy was chosen so as to maximize the X-ray flux while keeping a good discrimination between the diffraction patterns of different NPs (see [19], Fig. 4). The 2θ-zero error is estimated at 0.01°, yielding a negligible maximum error of 0.05% on the transferred momentum $q = 2\sin(\theta)/\lambda$.

3 The method

3.1 General features

In the traditional Rietveld method, the powder diffraction pattern of polycrystalline samples is composed of sharp Bragg peaks on a smooth background. It requires suitable models of: (i) crystal structure of all present phases; (ii) all sample-related effects (size, strain, disorder, preferred orientations, *et cetera*); (iii) instrumental contribution. For fcc-derived NPs, meaningful differences related to size reduction effects have to be considered.

Firstly, instrumental contributions are negligible due to the small NP size. Secondly, fcc-derived NPs often belong to non-periodic structure types[2]. Thirdly, the "lattice" parameters are size-dependent.

A novel approach [19] based on a Rietveld-like method implements these features. It takes into account three main structure types (cuboctahedron ($\mathcal{C}$), icosahedron ($\mathcal{I}$) and decahedron ($\mathcal{D}$)), which are made dimensionless (thereby independent of the specific material) by setting the nearest-neighbour distance (NND hereafter) equal to $1/(2\frac{1}{2})$. The Debye function (which does not require periodicity) is used to compute the diffracted intensity[3]. Additional features include a log-normal size distribution, as it is very commonly found in NPs [25], and an arctangent-like size-strain[4] dependence for each structure type (see [19] and supplementary material). The latter was chosen for its flexibility in representing a large variety of strain dependences, as shown in the following.

A new item here included (cf. Sect. 5) is an amorphous metal scattering contribution, based on a simplified model, for the background. This has been revealed a critical improvement as we found that an amorphous scattering is not well reproduced by low-order generic background-fitting functions (as Young's polynomials [26] used in the original work).

3.2 Disorder and strain in a nanoparticle

We have chosen to describe disorder and strain in NP [19] without considering the effect of 'classical' defects (e.g. vacancies, stacking faults, ...) and in particular the related Warren-Averbach (WA hereafter) effect (diffraction order-dependent Bragg peak broadening [27–29]). There

[2] These may also be referred to as multi-twinned particles or MTPs [1–4].

[3] We used a computationally feasible variant. In fact, the number of interatomic distances is $\propto D^6$ (D is the NP diameter). However, as we discussed in [19], all the information may be encoded in a number of sampled distances which is $\propto D$.

[4] Strain is approximated as uniform and isotropic *inside each single NP*.

are several reasons for that. Firstly, in this paper we deal with NPs of 4 to 36 nm^3 and it becomes unlikely to find more than a few defect (if any) in such small volumes. In particular, higher-energy defects (e.g. vacancies) may be disregarded, as the configurational entropy stabilization effect is negligible due to the small number of possible defect sites in one NP. Lower-energy defects (e.g. stacking faults) might instead be present and are sometimes observed [5]. We intend to introduce in a near future stacking faults contributions as in [29–31]. However, the samples here examined (see [17]) apparently do not contain a large occurrence of this kind of defects. Note that if dislocations are not likely present it is unnecessary to think about a dislocation-related WA effect.

Secondly, let's consider the effect of the surface. This is the most important source of disorder in small NPs. For NPs of 2 to 4 nm in diameter, 25% to 50% of the atoms are on the NPs' surface. Thiol-capped NPs are produced in solution, in the presence of thiol (ligand) molecules, which control particles' growth. In some cases, the surface layer may not be completely formed and may be very disordered or even amorphous, as it has been shown in simulations [22,32,33]. This is an important effect that had to be taken into account in our method, as described in the following sections. Furthermore, a tensile or compressive deformation of the underlying ordered core has to be considered. Similar mechanisms can be envisioned when two or more NPs randomly coalesce during the growth. Even when a perfectly structured NP is formed, interactions of surface atoms with the substrate/ligand likely produce a surface layer deformation (a radial compression or expansion), which propagates – more or less attenuated – to the NP core. Several reports have confirmed that (see Sect. 4.1). In short, we may assume that the 'lattice parameter' (more precisely, the bond length(s)) varies continuously from the center to the surface of the NP.

Our simple choice [19] was to describe the effect of this surface-led deformation as an average uniform and isotropic linear dilatation (compression or expansion, depending on sign) plus the static random disorder (incorporated in the Debye-Waller factor). Highly disordered surface layers are treated as amorphous and suitably accounted for. Again, we do not need to consider WA-like disorder-induced broadening because this is not justified for surface-led radial deformations described before. To understand this point, we have to recall some details. All information about the spherically averaged (powder) diffractivity of a cluster is encoded [19, 34] into its set $\{d;\mu\}$ of interatomic distances d and relevant multiplicities μ. Considering an ordered cluster with a given structure, the interatomic distance d corresponds to μ atom pairs at positions $(\boldsymbol{r}_1,\boldsymbol{r}_2),(\boldsymbol{r}_3,\boldsymbol{r}_4),\ldots$ (for convenience all atomic position vectors are referred to the cluster's center of mass). If the cluster is slightly deformed, all position vectors $\boldsymbol{r}_1,\boldsymbol{r}_2,\boldsymbol{r}_3,\ldots$ will change; for a radial deformation only their lengths will change. The atom pairs formerly related by d will now give a set of slightly different distances $\{d'\}$. We shall consider the average $a_d=\langle d'\rangle$ and variance $\sigma_d^2=\langle d'^2\rangle-\langle d'\rangle^2$ of this set as a function of the unperturbed common distance d. a_d is commonly assumed to be $\propto d$, preserving periodicity even if with slightly different lattice parameters. Crist and Cohen [35] have shown that WA broadening is directly related to σ_d^2 being proportional to d. This linear dependence causes order-dependent Bragg peak broadening, while a constant variance σ_d^2 would be seen as an increased Debye-Waller factor, reducing peak height without affecting the shape.

In the special case we are interested in this assumption fails. If we deform the cluster radially, with maximal deformation at the surface (as described above), it is possible to show – as we shall in a separate paper – that a) the average $\langle d\rangle$ is approximately proportional to d and, b) that the variance σ_d^2 has a complex dependence on d (increasing with d^2 at small d, smooth in the intermediate range and *decreasing* quadratically at high d). The latter behaviour is better described by a constant than a linear dependence. This justifies our approach.

3.3 Strain dependence on nanoparticle size

We refer to 'strain' as an uniform and isotropic dilatation of a NP[5] and originated in its surface deformation. Due to the strong size dependence of the surface effects, we expect a dependence of the strain profile on NP size. However, a full description of how it varies as a function of particle size is still unknown. To tackle this issue, we have tried different models of strain-size functional dependence, starting from constant to a doubly-curved function (arctangent). Section 4 presents a thorough study of such dependence based on our datasets.

3.4 Data analysis

Least-squares techniques were used to fit the experimental data. Model parameters are mass fractions, size and strain distribution together with background coefficients and an isotropic thermal factor. In our first formulation, a Gauss-Newton algorithm with quadratic line-search was used to minimize the residual norm. In order to better deal with the strong nonlinearity of the problem, this minimization algorithm has been now updated to a full-Newton method with analytical Hessian and saddle-point eliminations with a suitable recursive higher-order line search (see e.g. [36] and [37]) and an optional preliminary simplex stage [38].

4 Possible models of strain dependence on size

4.1 Former reports

Theoretical Density Functional Theory calculations [20] as well as Molecular Dynamics calculations [21, 39] on surfactant-free Au NPs indicate a contraction of the Au-Au NND (with respect to the bulk-Au value $d^0_{\mathrm{Au}}=0.2884$ nm [40]) when decreasing the particle size

[5] Many authors prefer to speak of 'lattice parameter' in this case, but a lattice parameter is ill-defined for non-periodic structures.

(about 4% at 1 nm diameter). Cleveland et al. also investigated thiol-capped Au NP samples by means of a limited comparison with experimental XRD patterns, highlighting a net expansion (1–2%) at 1–2 nm diameter [21] and a small contraction (half the predicted value) at 2–3 nm diameter [39]. This suggests caution in comparing theoretical and experimental data, especially because of the unpredictable influence of surface and interface interactions on energetically competitive structures. A recent work [41] clarified the role of the thiol molecules in relaxing the Au-Au distance. Vogel et al. [16] analysed Au NPs of about 1 nm embedded in an organosilicon polymer matrix, by XRD and EXAFS. A series of annealed samples, showing increased NP size, has also been studied. In their work, the NND was refined by least-square minimization of the XRD patterns, including a step-like strain size dependence, common to all samples (the step is arbitrary set to 575 atoms). The XRD analysis showed an average contraction of the Au-Au distance of about 3% with respect to the bulk value. EXAFS confirmed these results but indicating a stronger contraction of about 4–6%.

4.2 Modelling strain-size dependence

As mentioned, some attention has been devoted to investigate strain-size relationships but a robust methodology to extract strain information from XRD patterns is still needed. Here, we try to move forward in this direction by carrying out a detailed supplementary work to assess different models of strain-size dependence (shortly, 'strain models') with increasing complexity.

Cluster 'size' is represented (according to the shell-by-shell construction of [19]) by the number of shells n, proportional to the NP diameter D. To describe how strain depends on n, a flexible variably-smoothed arctangent-like function was used, considering four free parameters (Ω, Ξ, n_0, w) for each of the three structure types (see [19], Eqs. (9, 10)). Ω is the strain value at infinite size, Ξ is the strain value at the smallest possible size, n_0 is the size where the arctangent has its inflexion point, w is the arctangent rise width. Note that, for type $\mathcal{C}$, it is an immediate choice to set strain to 1 when the NND is equal to its value in bulk Au (d^0_{Au}). $\mathcal{I}$ and $\mathcal{D}$ have no "bulk" equivalent and are non-periodic. Furthermore, the NND in both types is very close to the bulk value (+6% in $\mathcal{I}$, +1% in $\mathcal{D}$). Our reference setting (strain = 1) is such that the NND of every structure type is equal to d^0_{Au}.

By using different combinations of the parameters to be refined, the arctangent can mimic simpler functions. For instance, fixing $\Xi = \Omega$ we obtain a constant, while setting w to a very high value and n_0, fixed, close to the mode of mass distribution we obtain a linear dependence. Accordingly, for each one of the three samples we performed repeated refinements with four strain-size complexity stages, as below:

1. CFS (Constant Fixed Strain): strain independent from size, with a *fixed* value for every structure type, scanning several possible combinations of values;
2. CVS (Constant Variable Strain): strain independent from size, with a *variable* (refined) value for each structure type;
3. LVS (Linear Variable Strain): linearly size-dependent strain with two refined parameters for each structure type;
4. FVS (Fully Variable Strain): full arctangent-like size-strain dependence with all four refined parameters for each structure type.

In the CFS stage the careful exploration of phase space is meant to provide a validation of refinement results in the absence of independent measurements, as it is advisable when a method and a model are tested for the first time. The strain factor (for each structure type) in this case is identified by the Ω parameter (with $\Xi = \Omega$ and n_0, w irrelevant). We selected 80 trial combinations of Ω values spanning[6] $\Omega = 0.99(0.01)1.03$ for $\mathcal{C}$ structure type and to $\Omega = 0.98(0.01)1.01$ for $\mathcal{I}$, $\mathcal{D}$ types. The "unstrained" case corresponds to set $\Omega = 1$ for all structure types. For each combination the starting set of parameters was completed by a trial assignment of the initial size distributions. Background was represented by Young polynomials with four coefficients for the 2.0 and 3.2 nm samples, and six for the 4.1 nm sample (a rather flat and featureless blank had been experimentally observed). Thereafter, for each combination least-squares minimization runs were performed to define the best values for all parameters (including Debye-Waller factors). The corresponding final goodness-of-fit (GoF) were computed and plotted in Figure 1 vs. the mass fractions of the three structure types. Note the broad variability in the final GoF range (showing the sensitivity of XRD data to strain) and the large variability of the refined mass fractions (showing the difficulty in obtaining a correct estimate of the latter when the strain is not known). For all samples, few results corresponding to the lowest GoF values can be distinguished from the others (see lower half of Fig. 1, together with the relevant Ω combinations). We can observe that the lowest GoF values increase with the sample cluster size, which indicates a greater inadequacy of the constant strain model for larger nanoparticles. The best-GoF Ω combinations found in the CFS stage and the remaining parameters were taken as the starting set for the CVS stage. For the more complex LVS stage, the starting point was chosen as the final point of CVS. In the FVS case, the starting point was obtained by a preliminary stage of simplex-method minimization [36, 38].

4.3 Comparison of results with different strain models

In Table 1 we present the refined values of the mass fractions of each structure type obtained by CVS, LVS and FVS, respectively, and the final GoF value of each run. We can observe:

1) GoF values always decrease from CVS → LVS → FVS for each sample, reaching good values for 2.0 nm (GoF = 1.045) and 3.2 nm samples (GoF = 1.112),

[6] Notation: lower bound(step)upper bound.

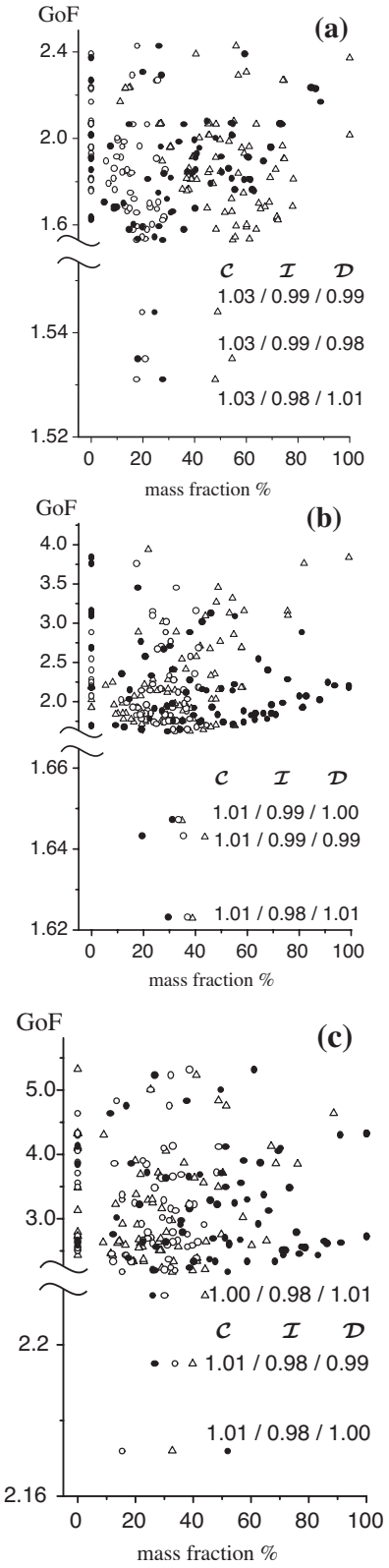

Fig. 1. The GoF values vs. the % mass fraction obtained from least-squares refinement for different combinations of fixed $\Omega \equiv \Xi$ strain parameters (CFS, cf. Sect. 4.2) for $\mathcal{C}$ (○), $\mathcal{I}$ (△) and $\mathcal{D}$ (●) structure types in 2.0 nm (a), 3.2 nm (b) and 4.1 nm (c) samples. Ω triples corresponding to the best solutions are given.

Table 1. The mass fractions (%) of each structure type obtained by the strain models CVS, LVS, FVS (see Sect. 4.2) are reported for the three investigated samples. The final GoF value of each run is also presented. Standard deviations are reported below each value.

	2.0 nm			3.2 nm			4.1 nm		
	CVS	LVS	FVS	CVS	LVS	FVS	CVS	LVS	FVS
$\mathcal{C}$	6.8	11.8	18.1	38.5	38.9	29.9	24.4	29.0	26.9
±	0.2	0.2	1.1	1.1	1.3	0.7	1.3	1.5	1.4
$\mathcal{I}$	64.5	58.4	48.1	43.9	36.9	18.7	35.8	33.2	26.4
±	1.1	0.9	1.6	1.7	1.4	1.2	2.3	4.5	1.4
$\mathcal{D}$	28.7	29.8	33.8	17.6	24.2	51.4	39.8	37.8	46.7
±	1.2	0.9	1.5	1.7	1.9	1.5	2.6	2.1	1.9
GoF	1.14	1.05	1.05	1.59	1.51	1.12	2.06	1.90	1.82

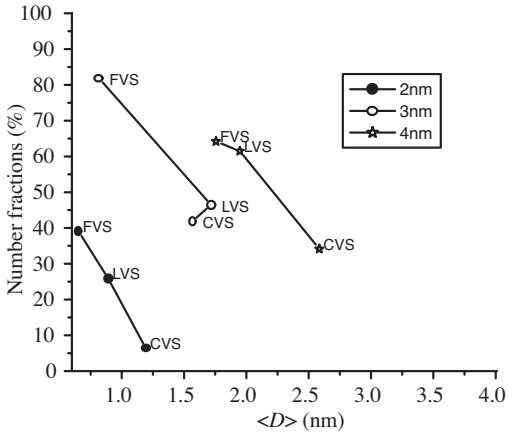

Fig. 2. Numerical fractions % of $\mathcal{C}$ structure as obtained for the three variable strain models (CVS, LVS, FVS, cf. Sect. 4.2) vs. the mean domain diameter $\langle D \rangle$, for the three investigated samples.

while still remaining unsatisfactory for the 4.1 nm sample (GoF = 1.820). Although similarities are found among the CVS/LVS/FVS results, FVS emerges as the most suitable when the size distribution is broad enough to justify it. In fact, as GoF values show, LVS and FVS are equivalent for the 2.0 nm sample, at least for $\mathcal{C}$ and $\mathcal{I}$, which have a very narrow size distribution.

2) Structure populations show broad variations within a single sample depending on the applied strain model.
3) Unrelated to the strain model and to the sample, $\mathcal{C}$ always shows a very high and unreasonable tensile state (from +30% to +5%) for the smallest clusters (≤1 nm). $\mathcal{I}$ always has strain <1, as expected.

The previous analysis gives some convincing results, but some doubtful aspects still remain. In particular, the high dilatation in the smallest $\mathcal{C}$ clusters of all samples seems unreasonable. Indeed this behaviour is also coupled with a given trend of the $\mathcal{C}$ size distributions with respect to the GoF values, as shown in Figure 2, where the numerical

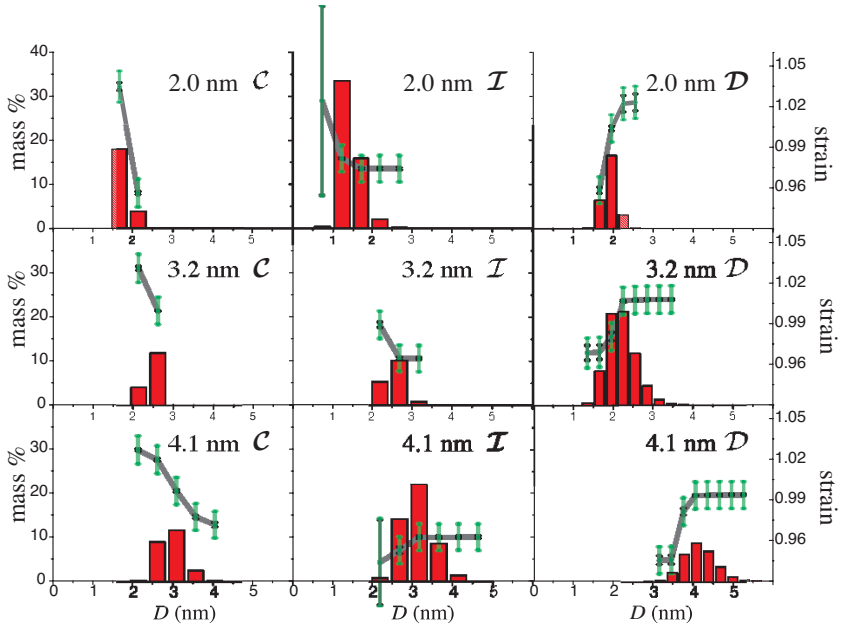

Fig. 3. Final size and strain distributions of $\mathcal{C}$, $\mathcal{I}$ and $\mathcal{D}$ structures in the 2.0, 3.2 and 4.1 nm samples, respectively. % mass fractions and strain-size profiles are given vs. the domain diameter.

fraction % of $\mathcal{C}$ corresponding to CVS, LVS and FVS in the three samples is plotted vs. the mean sample domain size. This figure clearly indicates the increasing abundance of very small "$\mathcal{C}$-like" domains with high deformation when passing from CVS → LVS → FVS strain models (i.e. with decreasing GoF). This trend has been interpreted as the effect of an amorphous fraction in the samples whose diffraction is not well modeled. The next section addresses how we tackled this problem.

5 Final results and discussion

According to the previous analysis, a simple amorphous metal-like background contribution was introduced. The HRTEM analysis in [17] gave evidence of disordered and partly ordered clusters in these samples, with possible imperfect surfaces. For noble metal (Au, Pd) NPs this is a known possibility. A pioneering work by [42] indicates the possible existence of a "liquid" surface layer on 20–50 nm diameter Au NPs. Experimental and theoretical studies (see DFT calculations in [22] and experimental studies cited therein) pointed out the stability of very small (≈55 atoms) amorphous Au or Pd NPs *in vacuo*. Note that 55 atoms correspond to $\mathcal{C}$- or $\mathcal{I}$-NPs with two shells. More interestingly, Molecular Dynamics calculations by [32] (see also [43]) on larger Pd clusters (>900 atoms, a 6-shell $\mathcal{C}$-NP of 3.2 nm diameter) show that the surface layer (one or two shells) of a perfectly ordered NP may tend to be amorphous. Figure 6 of [32] shows the contribution of such layer to the diffraction pattern. For the purpose of the present work, similar MD calculations are too heavy from the computational point of view. Therefore, we adopted a simpler approach to keep the perfect model structures but taking into account the diffractivity of amorphous surface layers.

Amorphous metals typically show the same local order as in bulk crystals but within a short range (below ≈1 nm). Therefore, to simulate the main features of an amorphous contribution, we took a linear combination of diffraction patterns from $\mathcal{C}$ clusters of one- and two-shell (with diameters of about 0.6 nm and 1.2 nm, respectively), each with an independently refined strain parameter and thermal factor. We stress that the aim of this operation was neither to provide a structural analysis of a possible amorphous phase nor its quantification, but only to add a suitable component to the background to minimize the error in the analysis by considering only ordered nanodomains. With the same purpose, the number of Young's polynomial coefficients for the remaining background intensity was increased to eight.

Another slight improvement in this model was the introduction of separate isotropic thermal parameters for each structure type. The total number of parameters were 24 for the NP spectrum plus 14 for background and amorphous scattering.

To test the influence of these corrections, following the indications given in Section 4.3, a new FVS least-squares refinement was carried out for all samples. Results show a consistent improvement, justifying the increased model complexity.

The final structure, size and strain distributions are presented in Figure 3 for all samples. In Table 2 the mass fractions (W), the mean diameter ($\langle D \rangle$) and the isotropic thermal factor (B) of each structure type, as well as the final GoF values are reported. Figure 4 shows the final best-fit for each sample together with the profile of the total background. The cumulative domain size distribution

Table 2. The mass fractions (W), the mean diameter ($\langle D \rangle$) of domains and the isotropic thermal factors B of each structure type corresponding to the final results are reported for the three investigated samples, together with the final GoF. W is expressed in % and $\langle D \rangle$ in nm.

	2.0 nm			3.2 nm			4.1 nm		
	W	$\langle D \rangle$	B	W	$\langle D \rangle$	B	W	$\langle D \rangle$	B
$\mathcal{C}$	21.8	1.8	6.0	15.8	2.4	0.2	23.8	2.9	0.2
$\pm$	0.8	0.4	0.6	0.9	0.4	0.1	1.5	0.6	0.1
$\mathcal{I}$	52.1	1.3	2.2	16.3	2.5	0.4	47.2	3.0	5.2
$\pm$	3.9	0.5	0.2	2.1	0.5	0.2	3.0	0.6	0.3
$\mathcal{D}$	26.1	1.9	1.4	67.9	2.0	2.6	29.0	4.0	1.2
$\pm$	3.2	0.3	0.2	4.4	0.5	0.1	3.5	0.5	0.2
GoF	**0.983**			**1.054**			**1.220**		

is given in the inset. First of all we outline the general improvement obtained, especially for the 4.1 nm sample (final Gof = 1.2) due to the new amorphous-like background correction. The fit is now as good as it could be and we have reasonable values of all refined parameters for all samples. More detailed and complex models for the amorphous background contribution are of course possible. However, with GoF ≈ 1 we have reached the limit of what we can obtain from these data sets. Tests of improved models are planned for new higher-quality data sets.

The cumulative size distributions in the insets of Figure 4 confirm that the average domain sizes of the three samples are systematically smaller than the NP size, as determined by HRTEM [17]. This finding can be ascribed to the occurrence of imperfectly formed NPs, probably with amorphous surface (cf. [32]). We cannot exclude multi-domain NPs (possibly including simple twins). However, as we can see from Figure 3, in all samples and for all structure types there is a fraction of NPs which match the nominal (HRTEM-inferred) NPs size.

The strain profiles of each structure type show a similar trend throughout the three samples, presenting a different deformation at the smallest and the largest size: $\mathcal{C}$ domains have a tensile strain (3%) at the smallest size and a compressive deformation (1–4%, in agreement with [20]) at the largest ones; $\mathcal{D}$ domains present opposite behaviour; $\mathcal{I}$ domains show a compressive lattice deformation (2–3%, again in agreement with [20]) at larger size but different trends towards the smaller sizes. These strain profiles agree well with the above discussed existence of both single-domain ordered NPs and imperfectly formed and/or multi-domain NPs. Amorphous surface or interface layers may play an important role as well, determining the average strain of smaller domains. Indeed, strain profiles seem to be more related to the synthesis process in each sample than to the particles size. This amorphous layer might also give rise to high tensile deformation of the whole NP.

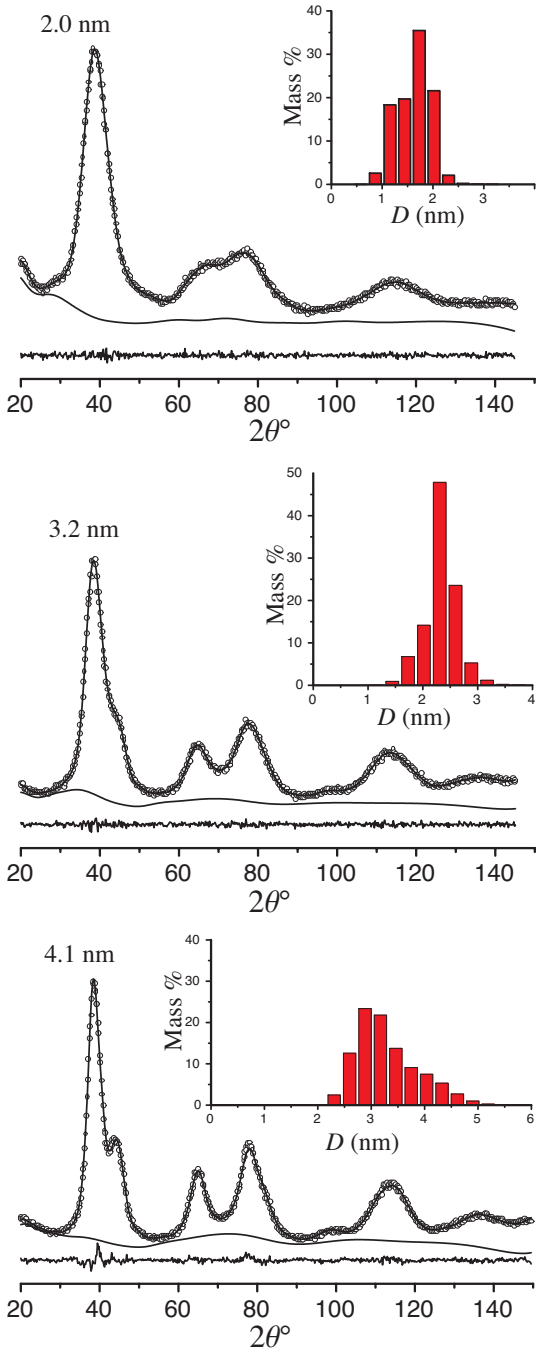

Fig. 4. XRD pattern best fit and cumulative size distribution (see insets) for the 2.0 nm (a), 3.2 nm (b) and 4.1 nm (c) samples. Experimental (circle) and calculated (solid line) intensities are plotted together with the total background profile (including the amorphous-like contribution) and the difference profile (below).

In this sense, the presence and position of a step on the strain-size profile may depend on the surface arrangement of a bulky surfactant. Additional studies are under way to clarify this behavior.

The derived strain profiles do not allow a straightforward assessment of the NND variations with respect to the bulk structure, when both structural and size dependences

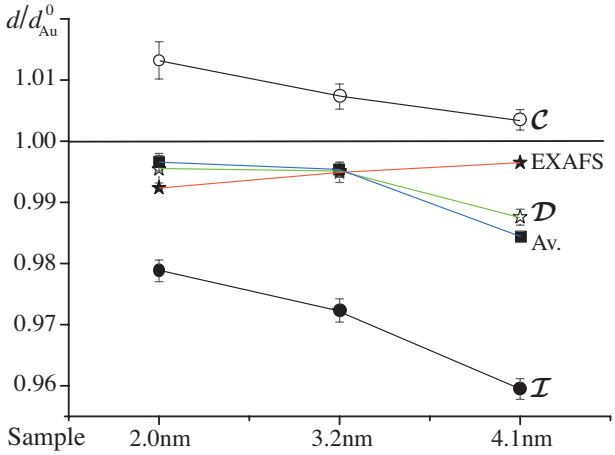

Fig. 5. Mean values of NND for each structure type and the sample average (Av.) for the 2.0, 3.2 and 4.1 nm samples. EXAFS NND values are taken from [24].

are accounted for. We remind again that in $\mathcal{I}$ and $\mathcal{D}$ the NND is very close to the bulk value (few % [19]), which belong to the same coordination polyhedron. Accordingly, the averages of the NNDs have been calculated for each sample, either distinctly for each structure type and as global sample average. These values have been normalized by the NND bulk value and plotted in Figure 5 for the three samples, together with values derived from EXAFS analysis [24] for comparison. Figure 5 clearly shows the dilatation of NND for $\mathcal{C}$ and the contraction for $\mathcal{I}$ and $\mathcal{D}$, which in sample averages results to a contraction. We see also the compressive trend of all structure types with increasing cluster size. This seems to be in good agreement with the relaxing effect of the thiol molecules on the inter-atomic distances of surface atoms described elsewhere [24, 41]. In fact, as the surface-to-volume ratio increases dramatically at smaller sizes, we can expect a major influence of the capping agent for the smaller size samples. Of course, NNDs values derived by the present XRD analysis refer to the "ordered" fraction in each sample. On the contrary, EXAFS results refer to the whole sample, including a not negligible amorphous fraction. Furthermore, the EXAFS–XRD comparison is rather delicate because of the complexity of the system. The NND is a complex average on many slightly different distances. Differences between XRD and EXAFS NNDs values and methods should be carefully considered, and further studies are under way to better address this issue.

Another aspect to be considered is the evolution of the structure populations through the three samples. A clear trend is not observed in the cumulative percentages given in Table 2, where the contributions of composite and single domain clusters are not distinguished. Additional information about the structure evolution with NP size can be drawn from the estimated thermal factor of each structure type, as indicators of possible structural disorder and relative stability. We can expect that $\mathcal{C}$ should not be very stable at the lowest sizes, as well as $\mathcal{I}$ at the largest sizes (cf. [5,16]). The high B values found for $\mathcal{C}$ in 2.0 nm sample and for $\mathcal{I}$ in 4.1 nm sample are in good agreement with these expectations.

6 Conclusions

This work describes a *simultaneous* extensive investigation on size distribution and strain-size dependence of thiol-capped gold NPs samples in the size range 2–4 nm based *only* on XRD data. Firstly, distributions of domain size and strain have been derived in these NP samples. Secondly, we highlighted the presence of an amorphous phase, as previously evidenced by HRTEM [17]. Concerning the method of analysis, an improvement of the background function has been implemented to achieve the best final results. Other systems and higher-quality data sets are under investigation to further test this methodology and corroborate the results.

References

1. S. Ino, J. Phys. Soc. Jpn **21**, 346 (1966)
2. S. Ino, S. Ogawa, J. Phys. Soc. Jpn **22**, 1365 (1967)
3. S. Ino, J. Phys. Soc. Jpn **26**, 1559 (1969)
4. S. Ino, J. Phys. Soc. Jpn **27**, 941 (1969)
5. L.D. Marks, Rep. Prog. Phys. **57**, 603 (1994)
6. D.A. Handley, *Colloidal Gold: Principles Methods and Applications,* Vol. 1 (Academic Press, New York, 1989), pp. 13–32
7. G. Schmid, A. Lehnert, Angew. Chem. Int. Ed. Engl. **28**, 780 (1989)
8. M. Brust, J. Fink, D. Bethell, D.J. Schiffrin, C. Kienly, Chem. Comm. **16**, 1655 (1995)
9. L.O. Brown, J.E. Hutchison, J. Am. Chem. Soc. **121**, 882 (1999)
10. L. Quaroni, G. Chumanov, J. Am. Chem. Soc. **121**, 10642 (1999)
11. L. Rivas, S. Sanchez-Cortes, J.V. Garcia-Ramos, G. Morcillo, Langmuir **17**, 574 (2001)
12. B.G. Erchov, N.L. Suchov, E. Janata, J. Phys. Chem. B **104**, 6138 (2000)
13. V.F. Puntes, K.M. Krishnan, A.P. Alivisatos, Science **291**, 2115 (2001)
14. V.F. Puntes, K.M. Krishnan, A.P. Alivisatos, Appl. Phys. Lett. **78**, 2187 (2001)
15. M.R. Diehl, J.Y. Yu, J.R. Heath, G.A. Held, H. Doyle, S.H. Sun, C.B. Murray, J. Phys. Chem. B **105**, 7913 (2001)
16. W. Vogel, J. Bradley, O. Vollmer, I. Abraham, J. Phys. Chem. B **102**, 10853 (1998)
17. D. Zanchet, B.H. Hall, D. Ugarte, J. Phys. Chem. B **104**, 11013 (2000)
18. B.D. Hall, J. Appl. Phys. **87**, 1666 (2000)
19. A. Cervellino, C. Giannini, A. Guagliardi, J. Appl. Cryst. **36**, 1148 (2003)
20. G. D'Agostino, A. Pinto, S. Mobilio, Phys. Rev. B **48**, 14447 (1993)
21. C.L. Cleveland, U. Landman, T.G. Schaaff, M.N. Shafigullin, P.M. Stephens, R. Whetten, Phys. Rev. Lett. **79**, 1873 (1997)

22. I.L. Garzón, A. Posada-Amarillas, Phys. Rev. B **54**, 11796 (1996)
23. A. Howie, L.D. Marks, Phil. Mag. A **49**, 95 (1984)
24. D. Zanchet, H. Tolentino, M.C. Alves, O.L. Alves, D. Ugarte, Chem. Phys. Lett. **323**, 167 (2000)
25. L.F. Kiss, J. Söderlund, G.A. Niklasson, C.G. Granqvist, Nanotechnology **10**, 25 (1999)
26. R.A. Young, *The Rietveld method,* edited by R.A. Young (IUCr, Oxford, 1993), Chap. 1 – *Introduction to the Rietveld method*
27. B.E. Warren, B.L. Averbach, J. Appl. Phys. **21**, 595 (1950)
28. B.E. Warren, B.L. Averbach, J. Appl. Phys. **23**, 497 (1952)
29. B.E. Warren, *X-ray diffraction* (Addison Wesley, Menlo Park, 1969), Chap. 13, pp. 251–314
30. G. Fagherazzi, A. Benedetti, A. Martorana, S. Giuliano, D. Duca, G. Deganello, Catalysis Lett. **6**, 263 (1990)
31. A. Martorana, G. Deganello, D. Duca, A. Benedetti, G. Fagherazzi, J. Appl. Cryst. **25**, 31 (1992)
32. Z. Kaszkur, J. Appl. Cryst. **33**, 87 (2000)
33. S.C. Hendy, J.P.K. Doye, Phys. Rev. B **66**, 235402 (2002)
34. A. Guinier, *X-ray diffraction in crystals, imperfect crystals, and amorphous bodies,* Reprint edn. (Dover Publications, Dover, 1994), Chap. 2, pp. 27–54
35. B. Crist, J.B. Cohen, J. Polym. Sci. Polym. Phys. Ed. **17**, 1001 (1979)
36. P.E. Gill, W. Murray, M. Wright, *Practical Optimization* (Academic Press, New York, 1981), pp. 59–154
37. J.E. Dennis, R.B. Schnabel, *Numerical Methods for Unconstrained Optimization and Nonlinear Equations* (SIAM, Philadelphia, 1996), pp. 86–167, 218–238
38. J.A. Nelder, R. Mead, Comp. J. **7**, 308 (1965)
39. C.L. Cleveland, U. Landman, M.N. Shafigullin, P.W. Stephens, R.L. Whetten, Z. Phys. D **40**, 503 (1997)
40. P. Villars, L.D. Calvert, *Pearson's Handbook of Crystallographic Data for Intermetallic Phases* (ASM, USA, 1991)
41. P. Zhang, T.K. Sham, Phys. Rev. Lett. **90**, 245502 (2003)
42. P. Buffat, J.-P. Borel, Phys. Rev. A **13**, 2287 (1976)
43. Z. Kaszkur, J. Appl. Cryst. **33**, 1262 (2000)